Two-photon interference : spatial aspects of two-photon entanglement, diffraction, and scattering

Peeters, W.H.

3

Optical characterization of periodically poled crystals

We demonstrate how the Maker fringes that are observable in spontaneous parametric down-conversion (SPDC) give a direct visualization of the poling quality of a periodically poled crystal. Identical Maker fringes are observed in the optical spectrum of collinear SPDC and the temperature dependence of second harmonic generation. We analyze these Maker fringes via a unified treatment of the tuning curve in crystals with small and slowly varying deformations of the poling structure. Our theoretical model, based on a Fourier analysis of the poling deformations, distinguishes between duty-cycle variations and variations of the poling phase. The analysis indicates that the poling phase is approximately fixed, while the duty-cycle typically varies between 36% and 64%.

W. H. Peeters and M. P. van Exter, *Optical characterization of periodically poled $KTiPO_4$*, Optics Express **16**, 7344 (2008)

3.1 Introduction

Phase matching is required for an efficient operation of second-order nonlinear optical processes such as second harmonic generation (SHG) and spontaneous parametric down-conversion (SPDC). In uniform crystals, phase matching is achieved by utilizing the modal dispersion resulting from the crystal's birefringence. Another method called quasi phase matching (QPM) relies on the fabrication of a ferroelectric domain structure with periodically inverting polarization. QPM allows for a larger choice of optical frequencies and allows access to more, and potentially larger, elements of the nonlinear $\chi^{(2)}$ tensor. An extensive discussion on the tuning and tolerances of QPM can be found in an article of Fejer *et al.* [89]. Different poling techniques are discussed in Refs. [90, 91].

The quality of the fabricated poling structure is generally characterized via imaging of the domain boundaries at the crystal surface. Important techniques comprise surface-charge selective etching [92], electrostatic force microscopy [93], secondary-electron microscopy [94], and piezoresponse-assisted atomic force microscopy [95]. Another way to characterize the poling quality is by studying the phase-matching conditions of a second-order nonlinear process like SHG or SPDC. Common techniques in this category use the wavelength dependence of the conversion efficiency of SHG [96,97]. A three-dimensional characterization of the poling duty-cycle has been demonstrated using ultrashort pulses and SGH [98]. A third technique characterizes the crystal structure by mapping the angle-frequency distribution of radiation that is generated via SPDC [99].

In this chapter we present high quality measurements and a detailed analysis of the ring-shaped angular SPDC pattern, generated in a periodically poled $KTiOPO_4$ crystal (PPKTP). Our analysis is very different from earlier results presented by Kitaeva *et al.* [99], as these authors analyze the large scale angle-frequency distribution of the SPDC pattern, whereas we concentrate on the fine structure close to phase matching. We also demonstrate that the same fringe pattern is present in the optical spectrum in collinear SPDC and the temperature dependence of SHG. We denote the observed patterns as Maker fringes, as the typical sinc-type intensity dependence was first discussed by Maker et al. [100]. We perform a meticulous comparison between the measurements and our theoretical predictions of the fringe shape, hereby using up to date knowledge of KTP's material properties. Finally, we analyze the observed fringe patterns in terms of small and slowly varying deformations of the periodic poling structure.

The paper is organized as follows. Section 3.2 gives a theoretical description of the temperature, angle, and wavelength dependence of the phase-matching condition in periodically poled crystals. Section 3.3 describes the three experimental setups that are used for (A) the measurement of the angular SPDC pattern, (B) the spectrum of SPDC light, and (C) the temperature dependent conversion effi-

ciency in SHG. Sections 3.4.1, 3.4.2, and 3.4.3 discuss the Maker fringes that are experimentally obtained via the three above-mentioned methods. In Sec. 3.5, we analyze the observed deviations from the ideal sinc-shaped Maker fringes in terms of small and slowly varying deformations of the poling structure. We hereby use a theoretical treatment, given in Sec. 3.5.1, that is based on a Fourier analysis of small and slowly varying deformations of the poling structure.

3.2 Phase matching in a periodically poled crystal

We consider the nonlinear processes of second harmonic generation (SHG) and spontaneous parametric down-conversion (SPDC) in a periodically poled crystal. For both processes, we assume loosely focussed cw-pumping (Rayleigh range pump $\gg$ crystal length) in the low conversion efficiency limit. The crystal is periodically poled along its crystallographic z axis in domains perpendicular to the crystallographic x axis. The pump beam is z polarized and propagates along the x axis. We consider the crystal to be infinite in the transverse directions. In the SHG configuration, we pump the crystal at angular frequency ω so that the up-converted wave has angular frequency 2ω. In the SPDC configuration, we pump the crystal at 2ω so that the angular frequencies of the down-converted signal and idler waves can be written as $\omega_s = \omega + \Omega/2$ and $\omega_i = \omega - \Omega/2$.

The SPDC process can be seen as the inverse process of SHG, when considering the same spatial and spectral modes. The conversion efficiencies of both processes (per spatial and spectral mode) are thus described by the same tuning curve, which is the conversion efficiency as a function of wave vector mismatch Δk along the x direction of the crystal. The tuning curve depends on the precise position-dependent nonlinear coefficient $d(x)$. More specifically, the conversion efficiency as a function of Δk is proportional to the absolute value squared of the Fourier transform of $d(x)$ [89].

An ideal periodically poled crystal has a square-wave-shaped nonlinear coefficient $d(x)$ with amplitude $\pm d_{\text{eff}}$, where the effective nonlinearity d_{eff} is a fixed material property. The Fourier transform of a square-wave-shaped $d(x)$ contains odd-m harmonics of the form $k_m^{\pm} = \pm 2\pi m/\Lambda_0$, where Λ_0 is the poling period of the crystal. Hence, the conversion efficiency will become peaked around any wave vector mismatch $\Delta k = k_m^{\pm}$. The mismatch parameter ϕ_m, defined as the accumulated phase mismatch over half the crystal length with respect to quasi-phase-matching order m, is

$$\phi_m = \frac{L_0}{2}\left[\left|\Delta k\right| f(T) - \frac{2\pi m}{\Lambda_0}\right], \tag{3.1}$$

where the crystal length L_0 and the poling period Λ_0 are specified at a certain reference temperature T_0. The function $f(T)$ is the temperature-dependent mate-

rial expansion factor which is defined to equal unity at the reference temperature. The conversion efficiency in the neighborhood of some m-order quasi phase match condition now becomes [89]

$$\eta_m(\phi_m) \propto \left(\frac{2}{\pi m}\right)^2 \mathrm{sinc}^2(\phi_m), \tag{3.2}$$

where the prefactor denotes the relative conversion efficiency, compared to the hypothetical case of a perfectly phase matched uniform crystal with an identical effective nonlinearity. The sinc function in Eq. (3.2) results from the Fourier transform of the hat-shaped crystal outline. In this chapter, we will restrict our analysis to quasi-phase-matching order $m = 1$, and we will drop the subscripts of ϕ_m and η_m. In accordance with Ref. [89] we normalize $\hat{\eta}(\phi)$ to its peak value via $\hat{\eta}(\phi) = \eta(\phi)/\eta(\phi = 0)$.

In order to calculate the mismatch parameter ϕ from Eq. (3.1), we must calculate the wave vector mismatch Δk along the x direction. The wave vector mismatch is defined as the wave vector of the 'blue' photon minus the wave vectors of the two 'red' photons. For the SHG configuration, this wave vector mismatch becomes

$$\Delta k_{\mathrm{SHG}} = k(2\omega, T) - 2k(\omega, T), \tag{3.3}$$

where $k(\omega, T)$ is the temperature-dependent dispersion relation of z polarized light in the crystal. Eq. (3.3) shows that the wave vector mismatch in SHG can be tuned in two different ways: via wavelength tuning and via temperature tuning. The wavelength and temperature dependence are often separated via

$$\begin{aligned} \Delta k_{\mathrm{SHG}} &= k(2\omega, T_0) - 2k(\omega, T_0) \\ &\quad + \frac{2\omega}{c}\big[\Delta n_z(2\omega, T) - \Delta n_z(\omega, T)\big], \end{aligned} \tag{3.4}$$

where $\Delta n_z(\omega, T) \equiv n_z(\omega, T) - n_z(\omega, T_0)$ is a shorthand notation for the change in refractive index caused by a deviation from the reference temperature $T_0 = 25\ ^\circ\mathrm{C}$ [101, 102].

The SPDC configuration differs from the SHG configuration in two ways. First of all, the signal and idler wave may have components in transverse directions. Secondly, any frequency difference $\Omega \equiv \omega_s - \omega_i$ between the signal and idler photon is allowed. Therefore, the wave vector mismatch in SPDC can be tuned in not just two, but four different ways: via wavelength tuning, via temperature tuning, via tuning of the detection angle, and via tuning of the detection wavelength. The wave vector mismatch in the SPDC configuration can be written as

$$\Delta k_{\mathrm{SPDC}} = k(2\omega, T) - [k_{s,x} + k_{i,x}], \tag{3.5}$$

where $k_{s,x}$ and $k_{i,x}$ are the x components of the wave vectors of the signal and idler waves in the crystal, respectively. Explicitly writing out the angle detuning and frequency detuning in the small angle and small frequency-detuning limit, yields

$$\begin{aligned}\Delta k_{\mathrm{SPDC}} &= k(2\omega,T) - 2k(\omega,T) \\ &\quad + k(\omega,T)\left[\theta_y^2 + \left(\frac{n_z}{n_x}\right)^2 \theta_z^2\right] \\ &\quad - \left.\frac{\partial^2 k}{\partial \omega^2}\right|_{\omega,T} \left(\frac{\Omega}{2}\right)^2, \end{aligned} \tag{3.6}$$

where $\boldsymbol{\theta} = (\theta_y, \theta_z)$ is the emission angle inside the crystal, and n_z and n_x are shorthand notations for the refractive index of z and x polarized light, respectively. The n_z/n_x factor in front of θ_z originates from the fact that down-converted light with a certain transverse k_z component carries a polarization with a small x component too. The angle dependence of the refractive index is found by using the index ellipsoid for our polarization. The latter term in Eq. (3.6) is obtained by performing a Taylor expansion around zero frequency detuning.

Throughout the article we will regularly use Eqs. (3.1)-(3.6) to compare our experimental results with existing literature on KTP's material properties. These properties involve Sellmeier dispersion equations [103–107], temperature dependence of the refractive index [101, 107, 108], and thermal expansion coefficients [101,102]. We will use the most recent and mutually most compatible literature values: the z component of the refractive index from Ref. [106], the x and y component of the refractive index from Ref. [107], the temperature dependence of the refractive index from Ref. [101], and the thermal expansion coefficients from Ref. [102].

3.3 Experimental apparatuses

Figure 3.1 shows the three experimental setups that we used for the characterization of the poling quality, either via SPDC [Figs. 3.1(a) and 3.1(b)] or SHG [Fig. 3.1(c)]. In this section we will give the experimental details of these three setups.

The pump part of the SPDC setups in Fig. 3.1(a) and Fig. 3.1(b) are identical. A cw krypton-ion laser (Coherent Innova 300) emits 220 mW at a vacuum wavelength of 413.1 nm in a TEM_{00} mode. This pump beam is mildly focussed ($w_0 = 190$ μm is the radius at e^{-2} of maximum irradiance) into a PPKTP crystal. The crystal is manufactured by Raicol Crystals Ltd. with low temperature periodic electrical poling, based on the application of a pulsed electric switching field to a patterned electrode [109]. The crystal has a length of 5.09 mm in the x direction, a thickness of 1 mm in the z direction and a width of 2 mm in the y direction. The pump beam propagates along the crystallographic x axis and is z polarized, allowing us to use

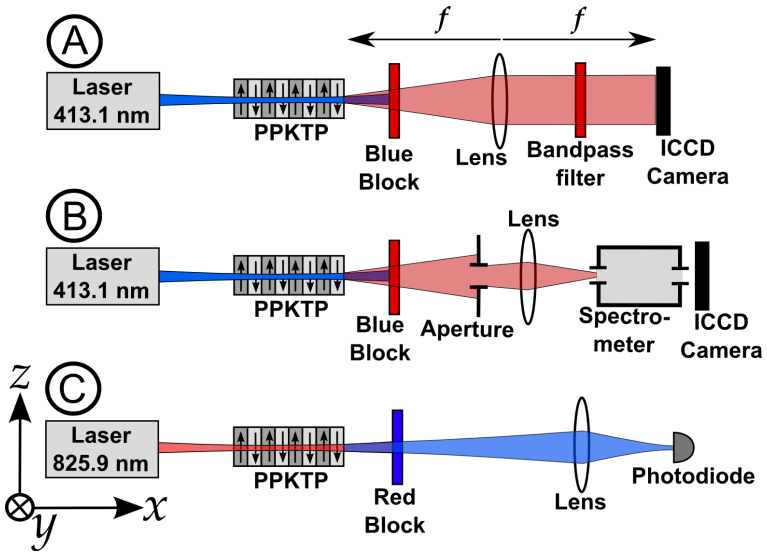

Figure 3.1: Three different experimental setups that are used to measure Maker fringes of a periodically poled $KTiOPO_4$ crystal (PPKTP). Setup A and B utilize the nonlinear processes of spontaneous parametric down-conversion, while setup C uses second harmonic generation. The indicated coordinate system corresponds to the crystallographic axes of the PPKTP crystal. Setup A: The far field of a narrow spectral band of the down-converted light is projected onto an intensified CCD camera (ICCD). Setup B: The spectral decomposition within a small angle (selected by the aperture) of the down-converted light is measured by placing an ICCD camera behind a spectrometer. Setup C: The power of the up-converted light is measured with a photodiode, while the crystal temperature is varied.

the large nonlinear d_{33} coefficient of KTP. The pump beam is centered on the crystal facets. The poling period of the crystal is specified to be $\Lambda_0 = 3.675$ μm which is designed for first-order quasi phase matching at 413.1 nm $\leftrightarrow$ 826.2 nm. The crystal is thermally contacted along the full crystal length to a bulky Aluminum mount via a 100 μm thick Indium layer. The temperature is stabilized to $\Delta T < 0.1$ °C using a Dale 1T1002-5 thermistor, an ILX-Lightwave LDT5910 controller and a Peltier element. The thermometer system is calibrated to an accuracy of $\pm(0.5\% + 0.2\ °C)$ by using a commercial ATAL RTD407907 thermometer. Phase matching in forward direction is achieved at a temperature of 60.7 °C.

The detection part of Fig. 3.1(a) contains a lens with focal length of 10 cm in an f-f geometry to project the far field onto an intensified CCD camera (ICCD) of Princeton Instruments (I-MAX-512-T,18). A narrow-band color filter selects a $\Delta\lambda = 5$ nm band around $\lambda = 826$ nm. This bandwidth is much smaller than the full width of the main Maker fringe in the spectral domain (see Fig. 3.5). The bandpass filter removes all angle-frequency correlations from the down-converted light.

The detection part of Fig. 3.1(b) contains an aperture that is positioned at large distance ($\simeq 0.5$ m) in the far field of the sample. The aperture selects a cone-shaped solid angle of 42 mrad^2 in the forward direction. The selected solid angle is much smaller than the solid angle of the main central Maker fringe (≈ 300 mrad^2), so that all angle-frequency correlations are removed. The light is then focussed onto the input slit of a spectrometer (Jobin Yvon 320) and the output is projected on an ICCD camera of Princeton Instruments (I-MAX-512-T,18). The dispersion of the spectrometer is 570 μm per nanometer. The width of the ICCD chip is 12.8 mm which corresponds to a full spectral width of a single image of $\Delta\lambda = 22$ nm. The center of the detected wavelength interval can be adjusted with a knob on the spectrum analyzer. The spectral response of the ICCD camera and spectrometer was calibrated by using a white light source and a non-intensified CCD with a well-specified spectral response. The spectrometer's offset was calibrated by using the 826.45 nm line of Argon.

The SHG setup in Fig. 3.1(c) is straightforward. A cw Ti:sapphire laser (Coherent 899 Ring Laser) emits 270 mW at a vacuum wavelength of 825.9 nm in a TEM_{00} mode. The beam is mildly focussed into the center of the same PPKTP crystal. The Rayleigh range of the beam is (14 ± 2) mm corresponding to a beam radius at e^{-2} of maximum irradiance of $w_0 = (61 \pm 4)$ μm. The pump propagates along the x direction of the crystal and is z polarized. The PPKTP crystal, the crystal mount and the temperature control part are the same as in the SPDC setup. The intensity of the SHG light is measured with a photodiode (HUV1100BQ), a homemade amplifier, and a voltmeter.

We have experimentally compared the peak conversion efficiencies of the 5-mm-long PPKTP crystal and a 1-mm-long β-BaB_2O_4 crystal (BBO). The conversion efficiency for both SPDC and SHG is expected to be much higher for PPKTP than for BBO. At a cutting angle $\theta_c = 29.2°$, the effective nonlinearity of BBO in type-I phase matching is expected to be $d_{\text{eff}} = -d_{22}\cos\theta_c = 2.0$ pm/V, based on data from Ref. [110]. For PPKTP, the effective nonlinearity corrected for first-order quasi phase matching is expected to be $(2/\pi)d_{33} = 9.8$ pm/V, based on data from Ref. [111]. When comparing crystals of equal length, it is thus expected that PPKTP yields $(9.8/2)^2 = 24$ times higher conversion efficiencies than BBO. In our case, the PPKTP crystal is 5 times longer than the BBO crystal, so we expect a conversion that is $5^2 \times 24 = 600$ times more efficient. We observe that the SHG process is approximately 575 times more efficient than the BBO crystal. In the inverse process of SPDC we observe an enhancement factor of approximately 700. Both observations are in reasonable agreement with the expected enhancement factor of 600. We conclude that the quality of the periodically poled crystal must be very good with a duty-cycle close to 50%.

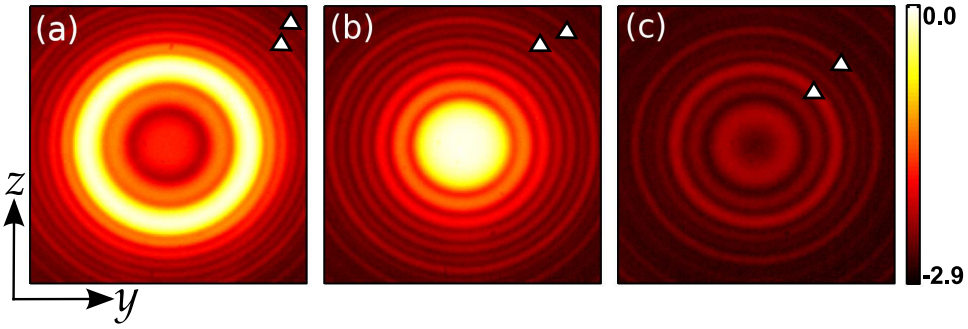

Figure 3.2: Measured angular intensity pattern of light generated via spontaneous parametric down-conversion in a 5-mm*-long periodically poled KTP crystal. The detection bandwidth is much smaller than the inverse angular dispersion of the Maker fringes. The color scale represents the logarithm (*$\log_{10}$*) of the intensity divided by the maximum intensity of the three images. The full width and full height of each image is* $96\ \text{mrad}$*. The three images are taken at different crystal temperatures: (a)* $53.5\ ^\circ\text{C}$*, (b)* $60.7\ ^\circ\text{C}$*, and (c)* $72.0\ ^\circ\text{C}$*. Phase matching in forward direction is achieved in situation (b). The sixth and ninth fringe stand out and are marked with triangles in each image. The same PPKTP crystal is used in Figs. 3.4, 3.3, 3.5, and 3.6. The fringe patterns are slightly elliptical.*

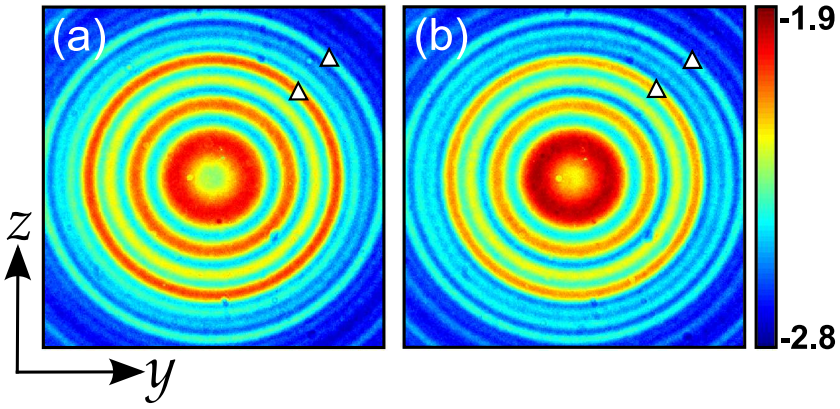

Figure 3.3: Measured SPDC ring pattern observed for pumping at two different positions on the crystal. The conditions are similar to those described in Fig. 3.2. The crystal temperature is now $69.7\ ^\circ\text{C}$ *and the image size is* $90\ \text{x}\ 90\ \text{mrad}^2$*. The pump positions on the crystal are separated by* $1.4\ \text{mm}$ *in the* y *direction. The images are very much alike. For instance, the sixth and ninth fringe stand out and are marked with triangles in both images. Only minor differences are visible. The patterns do not change upon a pump displacement in the* z *direction. The same PPKTP crystal is used in Figs. 3.2, 3.4, 3.5, and 3.6.*

3.4 Experimental results

3.4.1 Maker fringes in angular intensity pattern of SPDC light

The angular intensity pattern of light generated via SPDC in a 5-mm-long periodically poled KTP crystal is measured with the setup in Fig. 3.1(a). The details of the experimental apparatus are given in Sec. 3.3. Three images, taken at three different temperatures are presented in Fig. 3.2. The images contain Maker fringes [100] caused by the angle dependence of the phase-matching condition [see Eq. (3.6)]. We observe continuous expansion of the fringe pattern upon reduction of temperature.

Several important aspects of the images will now be discussed. First of all, the spacing between the successive rings decreases at large angles in such a way that $I \propto \mathrm{sinc}^2(A\Theta^2 + B)$, where Θ is the detection angle outside the crystal. The quadratic relation between detection angle and mismatch parameter is expected from Eqs. (3.6) and (3.1). Secondly, we observe that the ring pattern in Fig. 3.2 is slightly elliptical. This effect is due to a difference in the refractive index of z and x polarized light. Down-converted light with a certain k_z component has a polarization with a small x component, which causes the fringes to be elliptical [$n_z \neq n_x$ in Eq. (3.6)]. A third aspect concerns the peculiar deviations from the ideal sinc-like fringe structure. The sixth and ninth fringe, for example, are standing out with respect to neighboring fringes. These deviations are caused by small and slowly varying deformations of the poling structure. This experiment thus provides a simple and direct visualization of slowly varying deviations from perfect poling.

In order to quantify the ellipticity, we have performed some image processing. The image is first transformed from Cartesian coordinates to polar coordinates around the approximate center. Fourier analysis of this transformed image gives components of the form $f_l(r)\exp(il\varphi)$. The Fourier coefficients of this expansion depend strongly on the chosen position of the center. We have determined the optimal position of the center by minimizing the $l = 1$ coefficient. The ellipticity is now linked to the $l = 2$ coefficient of the Fourier expansion around this best center. We have accurately determined this ellipticity by stretching the image in the z direction until the $l = 2$ coefficient is minimized. This procedure is applied to 25 images taken at different temperatures between 45 °C and 72 °C. The resulting ellipticity is $n_z/n_x = 1.056 \pm 0.002$ where all the 25 different values are within the specified confidence region. Our measured value is in excellent agreement with existing literature giving $n_z/n_x = 1.0551$ [106, 107].

No ellipticity is left after the above-mentioned image stretching operation. This allows for rotational averaging which results in a single curve as a function of Θ_y^2 for each image. A composite curve, shown in Fig. 3.4, is generated by cutting, shifting, and pasting 25 rotationally averaged images taken at different temperatures. The main peak is shifted such that it coincides with the null of the Θ_y^2 axis. The result-

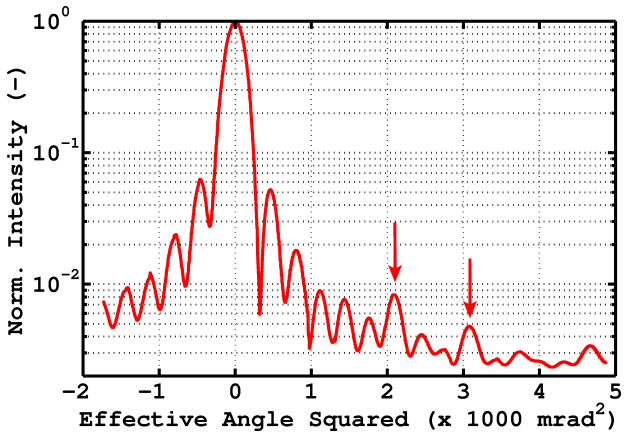

Figure 3.4: Composite plot of the measured angular intensity pattern of light generated via spontaneous parametric down-conversion in a 5-mm-*long periodically poled KTP crystal. The plot is obtained by combining 25 images of Maker fringes, like the ones shown in Fig. 3.2, photographed at different crystal temperatures ranging from* 45 °C *to* 89 °C*. The horizontal axis represents the square of the far field angle at a crystal temperature of* 60.7 °C*. The intensity values of the nodes have limited quantitative meaning (see text for details). The sixth and ninth fringe stand out and are marked with arrows. The same PPKTP crystal is used in Figs. 3.2, 3.3, 3.5, and 3.6.*

ing Θ_y^2 axis now relates without offset to the mismatch parameter ϕ in Eq. (3.2). Unfortunately, the node intensities in Fig. 3.4 have limited quantitative meaning as these intensities depend on the presence or absence of nearby bright fringes (see below).

The average distance between subsequent side lobes in Fig. 3.4 is measured to be $\Delta\Theta_y^2 = (325 \pm 8)$ mrad^2. The angular dependence of the phase-matching condition is theoretically described by Eq. (3.6). The measured external angle corresponds to the internal angle in Eq. (3.6) via $\Theta_y \approx n_z\theta_y$. The expected distance between subsequent side lobes thus becomes $\Delta\Theta_y^2 = 2\pi c n_z/L\omega = 299$ mrad^2 using the refractive index of Ref. [106]. We tentatively attribute the small discrepancy between the measured and the expected value for $\Delta\Theta_y^2$ to an unintended but possibly present 5% magnification in the imaging system.

Quite surprisingly, the minima in Fig. 3.2 do not go to zero, although all images have already been corrected for dark counts and stray light. The images in Fig. 3.2 and the curve in Fig. 3.4 have an offset of about $10^{-2.85} \approx 0.15\%$ of the peak intensity. The divergence of the pump laser of 0.7 mrad is too small to explain this observation. Additionally, we have observed that the intensity in a node is strongly reduced if we let a nearby bright fringe disappear from the image by increasing the temperature. For example, the intensity in the first minimum drops from 2.72% at

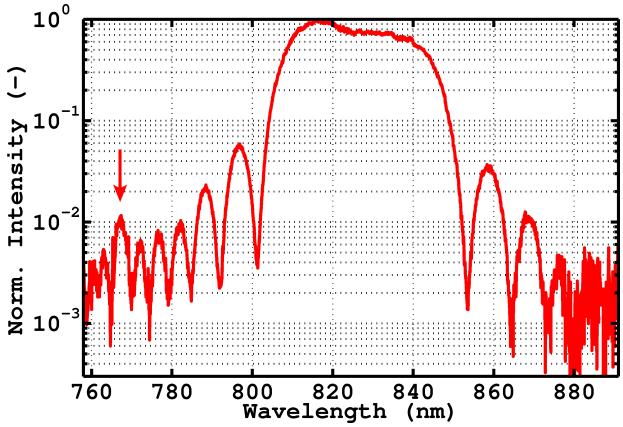

Figure 3.5: Spectrum of light generated via spontaneous parametric down-conversion in a 5-mm-*long periodically poled KTP crystal. The crystal is pumped by a mildly focussed beam at a wavelength of* 413.1 nm. *This spectrum is measured within a cone-shaped solid angle of* 42 mrad^2 *in forward direction. The crystal temperature is* 60.7 °C *at which phase matching is achieved in forward direction [see Fig. 3.2(b)]. The sixth fringe stands out and is marked with an arrow. The same PPKTP crystal is used in Figs. 3.2, 3.4, 3.3, and 3.6.*

$T = 60.7$ °C (collinear phase matching) to 0.56% at $T = 63.6$ °C, where the first minimum is in the forward direction. It thus seems that the intensity in a node is enhanced under the influence of nearby (bright) fringes. This effect can possibly be explained by a small degree of scattering from the crystal, predominantly in near-forward directions.

Characterization of the poling structure via the shape of the generated SPDC rings, is ideally suited for rapid inspection. We have applied this technique not only at the crystal center, but also over the full 1 mm x 2 mm cross-section of the crystal. This inspection reveals a large uniformity in both transverse directions. The observed ring patterns are almost identical at any position of the pump beam, including the prominent appearance of the sixth and ninth ring. The minor variation that we do observe occurs upon displacement in the 2 mm wide y direction and not in the 1 mm thick z direction. Two fringe patterns, corresponding to two pump positions that are 1.4 mm separated from each other along the y direction, are shown in Fig. 3.3. These images show the largest differences that we have observed, and even these are very small. The peak conversion efficiency (at phase-matching temperature) varies at most 2.5% over the y direction and only 1% over the z direction. We conclude that the observed deviations from perfect poling are present over the full cross-section, and show minor variations along the y direction.

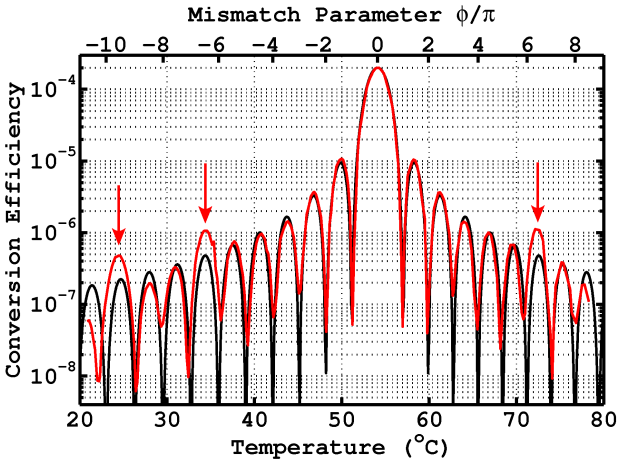

Figure 3.6: Red curve: measured temperature dependence of the conversion efficiency in SHG in a 5-mm*-long periodically poled KTP crystal that is pumped by a weakly focussed beam (*$w_0 = 61 \pm 4\ \mu\text{m}$*) at a wavelength of* $825.9\ \text{nm}$ *and a pump power of* $270\ \text{mW}$*. The nonlinear temperature dependence of the mismatch parameter* ϕ *is indicated by the nonequidistant markers on the* ϕ *axis on top of the figure. The sixth and ninth fringe stand out and are marked with arrows. The same PPKTP crystal is used in Figs. 3.2, 3.4, 3.3, and 3.5. Black curve: plot of the ideal non-deformed tuning curve of Eq. (3.2).*

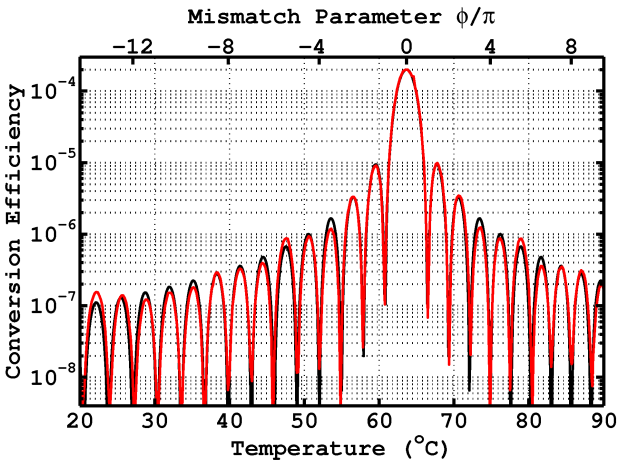

Figure 3.7: Red curve: measured temperature dependence of the conversion efficiency in SHG in a (different) 5-mm*-long periodically poled KTP crystal that is pumped by a weakly focussed beam (*$w_0 = 61 \pm 4\ \mu\text{m}$*) at a wavelength of* $826.4\ \text{nm}$ *and a pump power of* $270\ \text{mW}$*. The nonlinear temperature dependence of the mismatch parameter* ϕ *is indicated by the non-equidistant markers on the* ϕ *axis on top of the figure. Black curve: plot of the ideal non-deformed tuning curve of Eq. (3.2).*

3.4.2 Maker fringes in spectrum of SPDC light

The spectrum of the down-converted light of the same PPKTP crystal is measured with the setup depicted in Fig. 3.1(b). We have tuned the temperature to 60.7 °C so that phase matching is achieved in forward direction. Nine different spectral images between 760 nm and 890 nm have been recorded, each having a spectral width of $\Delta\lambda = 22$ nm. We have combined these images into a singe curve in Fig. 3.5 which thus represents the spectrum of the down-converted light. The observed spectrum contains Maker Fringes [100] as the curve's shape is governed by the phase-matching condition in the crystal.

The wave vector mismatch, given by Eq. (3.6), scales as the square frequency detuning $(\Omega/2)^2$. If we convert the λ axis into a $(\Omega/2)^2$ axis we find, as expected, a sinc-shaped tuning curve. The central peak is neatly centered around zero detuning which corresponds to a wavelength of 826.2 nm, being twice the pump wavelength. The spacing between subsequent side lobes is $\Delta(\Omega/2)^2 = (4.7 \pm 0.1) \times 10^{27}$ rad^2/s^2, which is in excellent agreement with the literature value of 4.69×10^{27} rad^2/s^2 derived from the Sellmeier equation in Ref. [106]. The fact that the mismatch parameter increases with the square of the frequency detuning causes the spectrum to be very wide, having a FWHM of about 34 nm even for a 5-mm-long crystal.

Again, we observe that the sixth side lobe is standing out with respect to the neighboring side lobes. This deviation is caused by small and slowly varying deformations of the poling structure. Finally, we observe that the Maker fringes on the red side are weaker than the fringes on the blue side. We tentatively attribute this unbalance to imperfections in the calibration of the spectral response of the spectrometer and the intensified CCD camera.

3.4.3 Maker fringes in temperature dependence of SHG

The temperature-dependent conversion efficiency of the SHG process in the same PPKTP crystal is measured with the setup in Fig. 3.1(c). The obtained result, shown in Fig. 3.6, contains Maker Fringes [100] as the curve's shape is again governed by the phase-matching condition in the crystal. The spacing between the subsequent side lobes decreases at large temperatures due the nonlinear relationship between temperature and refractive index of KTP [101]. Again, the sixth and ninth side lobe are standing out with respect to the neighboring peaks. These non-sinc-like features are caused by small and slowly varying deformations in the poling structure. We now achieve phase matching at a temperature of 54.1 °C, hereby using a pump wavelength of 825.9 nm. Phase matching in the SPDC experiments (see Fig. 3.2) was achieved at a different temperature of 60.7 °C because of the slightly longer relevant SPDC wavelength of 826.2 nm.

It is preferred to plot the measured Maker fringes as a function of mismatch

parameter ϕ rather than temperature. In order to make this conversion, accurate knowledge of the temperature dependence of the refractive index is needed. The temperature-dependent wave-vector mismatch in Eq. (3.4) is well described with two coefficients c_1 and c_2, defined via

$$\Delta n_z(2\omega, T) - \Delta n_z(\omega, T) = c_1[T - T_0] + c_2[T - T_0]^2, \tag{3.7}$$

because of the approximate quadratic temperature dependence of KTP's refractive index [101].

We have determined c_1 and c_2 from the measured tuning curve $\eta(T)$ by using the following procedure. The peaks and nodes of the measured tuning curve serve as markers for the mismatch parameter: $\phi = \pm(n + 1/2)\pi$ at the peaks and $\phi = \pm n\pi$ at the nodes. These markers yield the mismatch parameter ϕ at a number of temperatures. Coefficients c_1 and c_2 are obtained from a parabolic fit of Eq. (3.1) to the obtained set of mismatch parameters, after substituting Eqs. (3.7) and (3.4) into Eq. (3.1). In order to obtain reliable values for c_1 and c_2, we have applied this fitting method to five different PPKTP crystals. The tuning curve of one of these crystals is shown in Fig. 3.7. It closely resembles the ideal sinc^2-shape, thus showing that the poling structure of this second 5 mm long crystal is almost without any deformation. This curve is measured at a slightly longer pump wavelength of 826.4 nm instead of 825.9 nm causing phase matching to occur at 63.7 °C instead of 54.1 °C.

Our resulting coefficients are $c_1 = (24.0 \pm 0.2) \times 10^{-6}$ °C^{-1} and $c_2 = (4.8 \pm 0.3) \times 10^{-8}$ °C^{-2} at an approximate pump wavelength of 826 nm and a reference temperature of $T_0 = 25$ °C. The influence of the thermal expansion [102] on ϕ is only small ($\sim 4\%$) compared to the influence of the change in refractive index. The obtained coefficients are used to add a ϕ axis at the top of Fig. 3.6 and Fig. 3.7. The conversion from the measured $\eta(T)$ to the preferred form of $\eta(\phi)$ is now completed. We will use $\eta(\phi)$ for further analysis in Sec.3.5.

We now compare our values for c_1 and c_2 with existing literature. Reference [101] gives an explicit expression for $\Delta n_z(\omega, T)$ between vacuum wavelengths of 532 nm and 1585 nm. From this expression we calculate $c_1 = 23.56 \times 10^{-6}$ °C^{-1} and $c_2 = 8.6 \times 10^{-8}$ °C^{-2}. The c_1 coefficient is in reasonable agreement with our value, but there is a distinct discrepancy between the values for c_2. We conclude that it is inappropriate to extrapolate the expression for $\Delta n_z(\omega, T)$ in Ref. [101] to our pump wavelength of 413 nm. This wavelength is needed to calculate $\Delta n_z(2\omega, T)$ in Eq. (3.7).

Finally, we have measured the temperature dependence of SHG in five different PPKTP crystals of various lengths: 2 mm, 5 mm (two crystals), 10 mm, and 20 mm. The results of the two 5-mm-long crystals have already been presented in Figs. 3.6 and 3.7. For the three other crystals, the period of the sinc-pattern is inversely

proportional to the length of the crystal, as expected from Eq. (3.1). All crystals are of very high quality as the observed deviations from the ideal sinc-shape are even weaker than the features visible in Fig. 3.6.

3.5 Interpretation of Maker fringes in terms of poling quality

3.5.1 Fourier analysis of small and slowly varying deformations of the poling structure

An ideal periodically poled crystal has a sinc^2-shaped tuning curve. In practice, however, small deformations of the poling structure are often present, and such deformations reveal themselves as non-sinc-like features in the tuning curve $\hat{\eta}(\delta\Delta k)$. Fejer *et al.* [89] have analyzed the effects of various types of deformations on the tuning curve. In this subsection, we extend their treatment to a Fourier analysis of small and slowly varying deformations of the poling structure along the crystal. Faster deformations on a length scale of only a few lattice periods go unnoticed, as they are associated with very high harmonics that fall outside the experimental range of the observed Maker fringes. We make a clear distinction between slowly varying deformations of the poling phase and slowly varying deformations of the poling duty-cycle.

We consider second harmonic generation (SHG) and spontaneous parametric down-conversion (SPDC) under the conditions described in Sec. 3.2. The crystal length L_0 and the number of domains N relate to the design value of the poling period via $\Lambda_0 = 2L_0/N$. The tuning curve is peaked at any wave-vector mismatch Δk_0 obeying $|\Delta k_0| = 2\pi m/\Lambda_0$, where m can be any odd-valued quasi-phase-matching order. The positions of the domain boundaries required for perfect poling are $x_{n,0} = n\Lambda_0/2$.

Our analysis is restricted to imperfect positioning of the domain boundaries, i.e., to poling functions $d(x)$ that occupy two discrete levels $\pm d_{\mathrm{eff}}$. We specify the spatial deformations via the position error $\delta x_n \equiv x_n - x_{n,0}$ of the n_{th} domain boundary and introduce the phase error at the domain boundaries for fixed $\Delta k = \Delta k_0$ as

$$\Phi_n \equiv \Delta k_0 \delta x_n. \tag{3.8}$$

Note that our definition of Φ_n only contains the effects of the poling deformation. This definition differs from the one used by Fejer *et al.* [89], as their Φ_n also includes the accumulated phase due to the wave-vector mismatch $\delta\Delta k \equiv \Delta k - \Delta k_0$.

The conversion efficiencies of SHG and SPDC are affected by the poling deformations. The up-converted electric field in the process of SHG, normalized to the

field in case of perfect poling is [89]

$$\hat{E}(\delta\Delta k) \equiv \frac{E(\delta\Delta k)}{E_{\text{perfect}}} = \frac{1}{N}\sum_{n=1}^{N} e^{-i\delta\Delta k x} e^{-i\Phi_n}. \tag{3.9}$$

Next, we note that the poled crystal contains $N/2$ "building blocks" each consisting of two domains with opposite poling. Each building block is characterized by its length, being approximately equal to Λ_0, and its composition, i.e., the duty-cycle of the poling. The variations in these two quantities are related to the sum and differences of Φ_n and Φ_{n+1}. By introducing a slowly varying phase function $\Phi(x)$ and amplitude function $A(x)$ as

$$\Phi(\bar{x}_{n,0}) \equiv \tfrac{1}{2}(\Phi_n + \Phi_{n+1}), \tag{3.10}$$

$$A(\bar{x}_{n,0}) \equiv \cos\left[\tfrac{1}{2}(\Phi_n - \Phi_{n+1})\right], \tag{3.11}$$

where $\bar{x}_{n,0} \equiv (n + \frac{1}{2})\Lambda_0/2$, we can rewrite Eq. (3.9) as

$$\hat{E}(\delta\Delta k) \approx \frac{1}{L}\int_{-L/2}^{L/2} A(x) e^{-i\Phi(x)} e^{-i\delta\Delta k x} dx. \tag{3.12}$$

The complex amplitude $A(x)\exp[-i\Phi(x)]$ basically isolates the Fourier components of the two-level poling function $d(x)$ close to wave vector Δk_0. The phase function $\Phi(x)$ quantifies the displacement of the building blocks, whereas the amplitude function $A(x)$ is related to the duty-cycle of these blocks via $A(x) = \sin(\pi \times \text{dutycycle})$. The tuning curve, defined as the normalized conversion efficiency, is

$$\hat{\eta}(\delta\Delta k) = |\hat{E}(\delta\Delta k)|^2. \tag{3.13}$$

Equations (3.12) and (3.13) also apply to the SPDC process (per spatial and spectral mode), for which the wave-vector mismatch is calculated via Eq. (3.5).

Equation (3.12) exhibits the following symmetries. Deformations that are restricted to duty-cycle variations only, thus having $\Phi(x) = 0$, yield $\hat{E}(\delta\Delta k) = \hat{E}^*(-\delta\Delta k)$ and a symmetric tuning curve. Turning the crystal around corresponds to the operations $\Phi(x) \Rightarrow -\Phi(-x)$, $A(x) \Rightarrow A(-x)$, and hence $\hat{E}(\delta\Delta k) \Rightarrow \hat{E}^*(\delta\Delta k)$. Therefore, a measurement of the tuning curve $\hat{\eta}(\delta\Delta k)$ can not distinguish between the two possible crystal orientations. Symmetrically deformed crystals have real-valued $\hat{E}(\delta\Delta k)$.

For further analysis we expand the phase function $\Phi(x)$ and the amplitude func-

tion $A(x)$ in Fourier series as

$$\Phi(x) - \frac{a_0}{2} = \sum_{n=1}^{\infty} a_n \cos\left(\frac{2\pi n x}{L}\right) + b_n \sin\left(\frac{2\pi n x}{L}\right), \tag{3.14}$$

$$\frac{A(x)}{A_0} - 1 = \sum_{n=1}^{\infty} c_n \cos\left(\frac{2\pi n x}{L}\right) + d_n \sin\left(\frac{2\pi n x}{L}\right), \tag{3.15}$$

where a_n, b_n, c_n, and d_n are real-valued coefficients and $0 \leq A_0 \leq 1$ is the real-valued average amplitude. Any nonzero a_0 can be interpreted as a longitudinal displacement of the crystal, which is obviously neither an internal crystal property nor a parameter that influences the detected tuning curve. We shall assume small deformations $\Phi(x) \ll 1$, so that a first-order Taylor expansion of $\exp[-i\Phi(x)] \approx 1 - i\Phi(x)$ can be made. By inserting the Fourier decompositions in Eq. (3.12), and hereby neglecting second-order terms with amplitudes like $a_n c_n$, we find

$$\begin{aligned} \frac{\hat{E}(\phi)}{A_0} \approx\ & \operatorname{sinc}(\phi) + \sum_{n=1}^{\infty} \frac{c_n - i a_n + b_n + i d_n}{2} \operatorname{sinc}(\phi + n\pi) \\ & + \sum_{n=1}^{\infty} \frac{c_n - i a_n - b_n - i d_n}{2} \operatorname{sinc}(\phi - n\pi), \end{aligned} \tag{3.16}$$

where $\phi \equiv \frac{1}{2}\delta\Delta k L$ is the mismatch parameter. The dependence of the generated field on the wave-vector mismatch $\delta\Delta k$ is thus found to comprise a series of shifted sinc-functions with relative weights that contain essential information on the slow (= large scale) variations of the poling period. The tuning curve $\hat{\eta}(\phi)$ is symmetric with respect to $\phi = 0$ if at least all $b_n = 0$ in combination with either all $d_n = 0$ or all $a_n = 0$.

We will now calculate the values of the tuning curve at the positions of the peaks and nodes of the non-deformed sinc-function, as these give a good impression of the poling deformation. Inserting Eq. (3.16) into Eq. (3.13) we find

$$\hat{\eta}(\phi = \pm n\pi) \approx A_0^2 \left| \frac{\tilde{\alpha}_n \mp \tilde{\beta}_n}{2} \right|^2, \tag{3.17}$$

$$\hat{\eta}\left(\phi = \pm\left[s - \tfrac{1}{2}\right]\pi\right) \approx A_0^2 \left| \frac{1}{(s - \frac{1}{2})\pi} + \frac{\tilde{\zeta}_s \mp \tilde{\xi}_s}{2} \right|^2, \tag{3.18}$$

for the nodes and peaks, respectively. The complex $\tilde{\alpha}_n$, $\tilde{\beta}_n$, $\tilde{\zeta}_s$, and $\tilde{\xi}_s$ are linked to

the deformation coefficients as

$$\tilde{\alpha}_n \equiv (-1)^n\,[c_n - ia_n], \tag{3.19}$$

$$\tilde{\beta}_n \equiv (-1)^n\,[b_n + id_n], \tag{3.20}$$

$$\tilde{\zeta}_s \equiv \frac{2}{\pi}\sum_{n=1}^{\infty}\tilde{\alpha}_n\left[\frac{1}{2(s-n)-1}+\frac{1}{2(s+n)-1}\right], \tag{3.21}$$

$$\tilde{\xi}_s \equiv \frac{2}{\pi}\sum_{n=1}^{\infty}\tilde{\beta}_n\left[\frac{1}{2(s-n)-1}-\frac{1}{2(s+n)-1}\right]. \tag{3.22}$$

The $\{\tilde{\zeta}_s, \tilde{\xi}_s\}$ coefficients are uniquely determined by the deformation coefficients $\{\tilde{\alpha}_n, \tilde{\beta}_n\}$. The inverse transformations

$$\tilde{\alpha}_n = \frac{2}{\pi}\sum_{s=1}^{\infty}\tilde{\zeta}_s\left[\frac{1}{2(s-n)-1}+\frac{1}{2(s+n)-1}\right], \tag{3.23}$$

$$\tilde{\beta}_n = \frac{2}{\pi}\sum_{s=1}^{\infty}\tilde{\xi}_s\left[\frac{1}{2(s-n)-1}-\frac{1}{2(s+n)-1}\right], \tag{3.24}$$

and the following constraint

$$\sum_{s=1}^{\infty}\frac{\tilde{\zeta}_s}{2s-1} = 0, \tag{3.25}$$

can be derived from Eqs. (3.21) and (3.22). A sketch of this derivation and the physical interpretation of the coefficients are discussed in the final paragraph of this section. The fact that the inverse transformations exist, implies that both the $\{\tilde{\alpha}_n, \tilde{\beta}_n\}$-set and the $\{\tilde{\zeta}_s, \tilde{\xi}_s\}$-set individually contain all information on the poling deformations.

Equation (3.17) shows that the n_{th} node at each side of the main sinc-peak is determined by the $\tilde{\alpha}_n$ coefficient and $\tilde{\beta}_n$ coefficient only. This is because the maxima of the shifted sinc-functions in Eq. (3.16) coincide with the minima of the fundamental and all other shifted sinc-functions. The $\tilde{\alpha}$ coefficient affects both nodes in a symmetric way, whereas the $\tilde{\beta}$ coefficient can create an unbalance between the nodes. Equation (3.18) shows that the s_{th} side maximum at each side of the main sinc-peak is determined by the $\tilde{\zeta}_{(s+1)}$ coefficient and $\tilde{\xi}_{(s+1)}$ coefficient only. The reason being that $\tilde{\zeta}_{(s+1)}$ and $\tilde{\xi}_{(s+1)}$ are the coefficients of sinc functions that are shifted by $(s+1/2)\pi$, thus exchanging the role of minima and maxima. The $\tilde{\zeta}$ coefficient affects both side lobes in a symmetric way, whereas the $\tilde{\xi}$ coefficient can create an unbalance between the side lobes.

The transformation from the $\{\tilde{\alpha}_n, \tilde{\beta}_n\}$ coefficients to the $\{\tilde{\zeta}_s, \tilde{\xi}_s\}$ coefficients is related to a transformation from the Fourier basis $\{\cos[2\pi nx/L],\ \sin[2\pi nx/L]\}$ to an alternative basis comprising the shifted harmonic functions $\{\cos[2\pi(s -$

$\frac{1}{2})x/L],\ \sin[2\pi(s-\frac{1}{2})x/L]\}$. Apart from sign conventions, Eqs. (3.21)-(3.24) correspond to projections between those two function bases with an imposed zero-offset constraint. The explicit relation between the $\{\tilde{\zeta}_s, \tilde{\xi}_s\}$ coefficients and the poling deformations is

$$\Phi(x) - \frac{a_0}{2} = \sum_{s=1}^{\infty} \left\{ (-1)^s \mathrm{Im}(\tilde{\zeta}_s) \cos\left[\frac{2\pi\left(s-\frac{1}{2}\right)x}{L}\right] + (-1)^{s+1} \mathrm{Re}(\tilde{\xi}_s) \sin\left[\frac{2\pi\left(s-\frac{1}{2}\right)x}{L}\right] \right\}, \tag{3.26}$$

$$\frac{A(x)}{A_0} - 1 = \sum_{s=1}^{\infty} \left\{ (-1)^{s+1} \mathrm{Re}(\tilde{\zeta}_s) \cos\left[\frac{2\pi\left(s-\frac{1}{2}\right)x}{L}\right] + (-1)^{s+1} \mathrm{Im}(\tilde{\xi}_s) \sin\left[\frac{2\pi\left(s-\frac{1}{2}\right)x}{L}\right] \right\}. \tag{3.27}$$

The constraint in Eq. (3.25) ensures that the averages of the right-hand sides of Eq. (3.26) and Eq. (3.27) are zero.

3.5.2 Analysis of Maker fringes in terms of poling quality

As a typical experimental example we will analyze the measured tuning curve shown in Fig. 3.6 in a quantitative way. The poling quality of this crystal is very high as its tuning curve almost perfectly resembles the sinc^2-shape as given by Eq. (3.2). However, small deviations from the ideal curve are clearly visible, as, for example, the sixth and ninth side lobes are standing out with respect to the neighboring peaks. These non-sinc-like features are caused by small and slowly varying deformations in the poling structure that cover hundreds of poling periods. The reason is that the measured ϕ range covers about 20 sinc-nodes only, whereas the total amount of sinc-nodes in between two phase-matching orders, like $m = 1$ and $m = 2$, equals the number of domains which is about $2L_0/\Lambda_0 = 2770$.

An important ingredient of the Fourier analysis presented in Sec. 3.5.1 is the subdivision of the crystal into "building blocks", each block comprising two consecutive domains with opposite poling. The analysis distinguishes between variations of the poling phase, i.e., the longitudinal displacement of the building blocks, and variations of the poling duty-cycle that are related to the composition of the building blocks. The Fourier coefficients $\{a_n, b_n\}$, defined in Eq. (3.14), correspond to poling phase variations and the coefficients $\{c_n, d_n\}$ in Eq. (3.15) correspond to duty-cycle variations. We compare the experimental observations with our Fourier-model by first considering the effects of solely poling phase variations and afterwards considering the effects of solely duty-cycle variations.

We start by considering the effects of solely poling phase variations, mathemat-

ically corresponding to $c_n = d_n = 0$. This assumption is inspired by the fact that this category of deformations has a first-order effect on the tuning curve, whereas duty-cycle variations are only visible in second-order [see Eqs. (3.10) and (3.11)]. The symmetry with respect to $\phi = 0$ observed in Fig. 3.6 indicates that $b_n \approx 0$. The most prominent features are observed in the $\pm 6_{\mathrm{th}}$ and $\pm 9_{\mathrm{th}}$ side lobes (one outside figure). The tuning curve at the $\pm 6_{\mathrm{th}}$ peaks is measured to be $\hat{\eta} = 0.54\%$, whereas the expected value is only $\hat{\eta} = 0.24\%$. From these values and the assumption of an approximate constant duty-cycle, we find $\tilde{\zeta}_7 \approx \pm 0.11i$. The associated phase function $\Phi(x) = \pm 0.11 \cos(6\frac{1}{2} \times \frac{2\pi x}{L})$ corresponds to a periodic displacement of the domain boundaries by only $0.11\Lambda_0/2\pi m = 64$ nm over a typical period of $1/6\frac{1}{2}$ of the crystal length. This calculation shows that even very small variations in the poling phase have the potential to strongly enhance the intensities of the side lobes.

The assumption of an approximately fixed duty-cycle is however incompatible with the observation that the $\pm 3_{\mathrm{rd}}$ and $\pm 8_{\mathrm{th}}$ side lobes are lower than the expected peak height at both sides of the central peak. Equation (3.18) shows that a pair of side lobes can be lowered symmetrically, only if $\Re(\tilde{\zeta}) < 0$. Any nonzero real part of $\tilde{\zeta}$ is formed by nonzero c_n coefficients and thus by variations of the poling duty-cycle. We therefore conclude that the observed non-sinc-like features in Fig. 3.6 can not be caused by slowly varying deformations of the poling phase alone.

Next, we consider the effects of solely duty-cycle variations, mathematically corresponding to $a_n = b_n = 0$. This assumption is inspired by the fact that the observed tuning curve is almost perfectly symmetric, which is automatically the case when solely duty-cycle variations are assumed. Equation (3.18) gives the height of the side lobes, and it indicates that a real-valued $\tilde{\zeta}_s$ has a first-order effect on the side lobe strength, whereas an imaginary-valued $\tilde{\xi}_s$ has only a second-order effect. Therefore, it is possible to make a good estimate of $\{\tilde{\zeta}_s\}$ from the measured side lobe strengths alone. For example, from the measured $\pm 6_{\mathrm{th}}$ side lobes in Fig. 3.6, it is found that $\tilde{\zeta}_7 \approx 0.049$, corresponding to the amplitude function $A(x) = A_0[1 + 0.049 \cos(6\frac{1}{2} \times \frac{2\pi x}{L})]$. Assuming an average duty-cycle of 50%, the 9.8% variation in the amplitude function $A(x)$ corresponds to a duty-cycle variation between 36% and 64%. We thus find that the potential effect of duty-cycle variations on the tuning curve is relatively weak compared to the potential effect of poling phase deformations.

One might wonder whether or not it is possible to retrieve all deformation coefficients from a measurement of the tuning curve $\hat{\eta}(\phi)$. In general, it is not possible to do this inversion. For example, a sign-flip of all a_n and d_n coefficients will not change the outcome of the measurement. The large number of free parameters in the deformation model possibly limits the amount of retrievable information even further. Under some assumptions on the nature of the deformations, like the ones on duty-cycle variation discussed above, more stringent requirements on the ampli-

tudes of the deformations apply. Whatever the assumptions, the observed tuning curve always corresponds to a Fourier analysis of the amplitude function $A(x)$ and the poling phase function $\Phi(x)$. Non-sinc-like features in the tuning curve $\hat{\eta}(\phi)$ around the n_{th} side minimum must correspond to variations in $A(x)$ and $\Phi(x)$ with a typical period of L/n.

Finally, we summarize the above-described analysis on the nature and strength of the poling deformations. The approximate symmetry in Fig. 3.6 indicates that all $b_n \approx 0$. The measurement also proves that some c_n coefficients must be nonzero as some pairs of side lobes are lowered symmetrically at both sides of the main peak. In order to fully explain the observed symmetry in the tuning curve, it is also needed that either all $a_n \approx 0$ or all $d_n \approx 0$. We assume that $a_n \approx 0$, as we suppose that any realistic duty-cycle deformation mechanism would not distinguish between the c_n and d_n coefficients. We thus conclude that the poling deformations in the investigated PPKTP crystal comprise duty-cycle variations only. The stronger sixth side lobes in Fig. 3.6 correspond to a periodic 9.8% peak-to-peak variation in the amplitude function $A(x) = \sin(\pi \times \text{dutycycle})$.

It is likely that the origin of the variations of the duty-cycle lies in the fabrication process of PPKTP. The process for the fabrication of the domain pattern is based on electric field poling [112]. An important issue during the patterning process is domain broadening [109, 113]. The amount of domain broadening directly determines the duty-cycle, and hence domain broadening is likely to be the origin of the small deformations that we observe. Our observation in Sec. 3.4.1, that the poling deformations are the same at any z position of the pump beam, is consistent with the observation of Rosenman *et al.* [113], that domain broadening occurs dominantly in the first few microns close to the electrical contacts needed for the poling production.

3.6 Conclusions

We have demonstrated three different methods to measure the tuning curve of a periodically poled $KTiOPO_4$ crystal (PPKTP), utilizing the processes of spontaneous parametric down-conversion (SPDC) and second harmonic generation (SHG). The three methods concern a measurement of the angular intensity pattern of collinear SPDC light, the spectrum of SPDC light, and the temperature-dependent conversion efficiency in SHG. We have shown that the three methods are fully consistent, and that the outcomes are in agreement with current knowledge of KTP's material properties. We refer to the observed fringe pattern in the tuning curve as Maker fringes [100]. The angular intensity pattern of SPDC light directly visualizes the Maker fringes. We therefore consider this method to be an ideal tool to quickly characterize the poling quality.

The observed angular intensity pattern in SPDC exhibits two interesting aspects. First, we have observed that the fringe pattern is slightly elliptical, which is caused by the birefringence of KTP. The observed ellipticity of 5.5% is in excellent agreement with current knowledge of KTP's birefringence. Secondly, we observe that the images exhibit a small degree of fringe blurring and an offset intensity of about 0.15%. These two observations can possibly be explained by a small degree of scattering from the crystal, predominantly in near-forward directions.

Our measurements of the Maker fringes contain essential information about slowly varying deformations of the poling structure. These large scale imperfections of the poling structure manifest themselves as deformations of the tuning curve close to the point of perfect phase matching. We have developed a Fourier analysis for these deformations. An important ingredient of the analysis is the subdivision of the crystal into "building blocks", each block comprising two consecutive domains with opposite poling. The Fourier analysis distinguishes between variations of the poling phase, i.e., the longitudinal displacement of the blocks, and variations of the poling duty-cycle that are related to the composition of the building blocks. We give explicit expressions for the tuning curve, depending on the Fourier coefficients of the deformations. Our measurements of the tuning curve exhibit small non-sinc-like features. It is proven that these deviations can not be explained by slowly varying deformations of the poling phase alone. We show that the observed features are probably caused by variations of the poling duty-cycle alone. A specific feature in the observed tuning curve corresponds to a variation of the duty-cycle between 36% and 64%.

We have measured the angular intensity pattern of SPDC light for various pump positions on the crystal. The measurements reveal a uniformity in both transverse directions, as some prominent features in the fringe pattern are present at any pump position. Closer inspection, however, reveals a very small variation of the fringe pattern along the y direction of the crystal. We do not observe any variation of the fringe pattern along the z direction. The ferroelectric poling structure is fabricated via low temperature electrical poling, by applying a periodic electrode pattern on one of the polar z surfaces of the crystal. We conclude that the poling deformations must originate from close to the electrodes and remain uniform along the z direction of the crystal.

3.7 Acknowledgements

This work has been supported by the Stichting voor Fundamenteel Onderzoek der Materie. We thank A. Skliar for providing information about the crystals and the production process.